Magnetic behavior of two-dimensional Manganese Telluride

Chinmayee Chowde Gowda[1], Raphael Tromer[2], Prafull Pandey[3], Dharita Chandravanshi[4], Amreesh Chandra[5], Kamanio Chattopadhyay[3,4], Douglas S. Galvao[2,6 *], Chandra Sekhar Tiwary[1, 7*]

[1]School of Nano Science and Technology, Indian Institute of Technology Kharagpur, Kharagpur 721302, India
[2]Applied Physics Department, State University of Campinas, Campinas, SP, 13083-959, Brazil
[3]Department of Materials Engineering, Indian Institute of Science, Bangalore 560012, India
[4]Interdisciplinary Centre for Energy Research, Indian Institute of Science, Bangalore 560012, India
[5]Department of Physics, Indian Institute of Technology Kharagpur, Kharagpur 721302, India
[6]Center for Computational Engineering and Sciences, State University of Campinas, Campinas, SP, 13083-970, Brazil
[7]Department of Metallurgical and Materials Engineering, Indian Institute of Technology Kharagpur, Kharagpur 721302, India

E-mail: galvao@ifi.unicamp.br, chandra.tiwary@metal.iitkgp.ac.in

Received xxxxxx
Accepted for publication xxxxxx
Published xxxxxx

Abstract

Magnetism in atomically thin two-dimensional (2D) materials is attractive for several applications such as memory devices, sensors, biomedical devices, etc. Here, we have synthesized 2D manganese telluride (MnTe) using a scalable synthesis method consisting of melting followed by liquid phase exfoliation (LPE). Both bulk and 2D MnTe samples were analyzed for their magnetic behavior at room temperature and lower temperatures (10 K). A change from antiferromagnetic to paramagnetic behavior was observed in 2D MnTe flakes. Enhanced magnetic saturation values (up to 400% increase) were observed as compared to bulk MnTe in RT. Density functional theory (DFT) simulations explain the layer-dependent magnetic behavior of the 2D MnTe flakes, as well as the antiferromagnetic to paramagnetic transition due to an unbalanced spin population.

Keywords: 2D magnetism, Manganese telluride, Liquid phase exfoliation.

1. Introduction

Recent investigations have shown possible applications of transition metal dichalcogenides (TMDCs) for various magnetic field-based multifunctional applications. A few include spintronic devices with antiferromagnetic materials, antiferromagnetic topological insulators, sensing, and energy harvesting devices [1–4]. A change in magnetic behavior is often observed when the bulk material is confined to lower dimensions. Mermin-Wagner theorem has been set to explain the magnetism in lower dimensional materials [5]. Accordingly, continuous symmetries cannot be broken at finite temperatures in systems with sufficiently short-range interactions in dimensions $d \leq 2$. It means that long-range fluctuations can be created with little energy cost, and since they increase entropy, they are favoured. Doping, layered heterostructures, and other techniques can introduce magnetism to a material. It is known as intrinsic magnetism, and the induced magnetism by these

techniques is often weak and temporary. 2D material must have a highly anisotropic electronic structure to exhibit intrinsic magnetism. Dimensionality also plays a crucial role as the misaligned magnetic moments in long-range orders determine the critical temperature [6].

2D Manganese-based chalcogenides such as $MnSe_x$ and MnS_x (x=1, 2) have been theoretically predicted and experimentally studied extensively. MnSe and $MnSe_2$ have a rocksalt and pyrite structure (layered), respectively, and the low energies facilitate cleaving of these layers and thus reach the monolayer limit [7]. Moreover, $MnSe_2$ monolayers show out-of-plane ferromagnetic ordering [8]. Manganese tellurides are dilute magnetic semiconductors combining semiconducting and magnetic properties [9]. The sensitivity of magnetic coupling to atomic distance has been majorly observed in Mn-based materials, making them complex magnetic structures [10]. MnTe has a Ni-As type crystal structure, and magnetic behavior variations are observed as they reach lower dimensions. The material is known for its good thermoelectric properties though it has low electrical conductivity and considerable carrier concentrations. Studies show that the bulk MnTe is antiferromagnetic at room temperature (RT) and has a Curie temperature (T_c) at lower temperatures (40-50 K), and the Néel temperature (T_N) at about 310 K. 2D chalcogenides have shown paramagnetic behavior at 300 K (RT) [11]. Lower dimensional TMDCs (three atom thickness) have considerably varied properties compared to their bulk forms [12, 13]. Amongst them, magnetic field interaction and spin ordering vary drastically in these 2D structures [14, 15]. It is common to have abrupt changes in magnetic ordering for 2D systems. Thickness-dependent magnetic behavior of van der Waals solids, such as doped graphene, MoS_2, ReS_2, and Re-doped WSe_2, were also studied based on the long-range magnetic ordering effects on critical transition temperatures [16-18]. The magnetic behavior of the 2D MnTe has been of interest, as it exhibits a non-layered, non-van der Waals solid structure.

2.1 Material and methods

Manganese telluride (MnTe) alloys were made by flame melting under a continuous flow of ultra-pure argon. Stoichiometric amounts of 99.99% pure manganese and tellurium were taken based on Mn-Te binary alloy phase diagram. The melting point of MnTe is 1170 °C. The usage of acetylene flame achieved a higher temperature for melting. 10 g samples were weighed and melted in a 10 mm quartz tube. As the boiling point of tellurium (988 °C) is lower than the melting point of the alloy (1170 °C), proper mixing of the elements is ensured by keeping the sample at an elevated temperature of 950 °C for a longer duration. The samples were remelted 2-3 times to ensure homogeneity. The cooling of samples is performed under continuous argon flow in this process. Bulk MnTe samples were vacuum sealed and kept in a high-temperature furnace at 900 °C for homogenization. Gradual temperature increase until 900 °C over 2 hours was done and was kept at this temperature for 10 hours followed by furnace-cooling.

The bulk alloys were manually crushed and powdered using a mortar and pestle. The powders were then dispersed in propane-2-ol (IPA) extra pure (LR grade). The sample to solvent ratio was kept at 1 g: 200 ml. The bath sonication for 4 hours was carried out to exfoliate the samples. The solution of dispersed samples was rested for 48 hours. The supernatant was then collected and dried at 40 °C on a hot plate. The exfoliated powder sample thus obtained was used for further analysis. The schematic of the process is shown in **Figure 1a**.

Acetylene flame was used for flame melting to achieve higher temperatures. X-ray diffraction patterns and information on crystalline phases were analyzed using Bruker, D8 Advance X-ray diffractometer. Cu-Kα source of wavelength (λ) 1.5406 Å, operating at 40 kV voltage and 40 mA current, was used. Pearson's Crystal Database and Panalytical X'pert high score plus software were used for XRD structure data analysis. The optical absorbance property of bulk and exfoliated MnTe was characterized using a UV-visible spectrometer from 200 - 800 nm. The optical energy band gap was estimated using the Tauc plot method. Scanning electron microscopy (SEM) was performed using an SEM CARL ZEISS SUPRA 40, with a probe current up to 20 nA. We also used an electron probe microanalyzer (JEOL, JXA8530F) for energy dispersive x-ray spectroscopy analysis of samples. Transmission electron microscopy (TEM) was used to analyse the sample further. TEM imaging was performed in 60 – 300 kV low base Titan® Themis™ with a monochromator, a CEOS probe corrector for Cs aberration-corrected STEM, and a Quantum 965 Gatan Imaging Filter (post column) for EELS analysis. The samples were dispersed in IPA, a single drop (micro-pipette) was drop casted on formvar/carbon supported copper grid (200 mesh size) and desiccated before analysis. Atomic Force Microscopy (AFM) was performed using Agilent Technologies Model No 5500. The drop deposition technique was used for sample deposition on a monocrystalline silicon substrate.

Raman spectroscopy analyses were carried out using WITec UHTS Raman Spectrometer (WITec, UHTS 300 VIS, Germany) with a laser excitation wavelength of 532 nm at room temperature (RT). To investigate the materials' oxidation states and surface composition, an XPS ThermoFisher Scientific Nexsa was used, with Al-Kα radiation (λ=1486.71 eV) as a source. Differential Scanning Calorimetry (DSC) model Perkin Elmer 4000 was used to calculate the heat capacity of the material.

2.2 Theoretical Analysis - Methodology

We carried out Density Functional Theory (DFT) simulations to investigate the structural and magnetic properties of the 2D MnTe structures. A standard DFT approach was used to examine the properties of the structures with common semi-local approximations to the exchange-correlation energy combining the semi-local generalized gradient approximation (GGA) and the PBE functional [19]. We calculated the phonon spectra dispersion and used *ab initio* molecular dynamics (AIMD) to investigate the structural stabilities of 2D MnTe at T= 0 and 300 K. For the phonon dispersion calculations, we used the frozen phonon approximation and a Nosé thermostat. Both methods are implemented in the SIESTA software [20].

We considered for the theoretical analysis the 2D MnTe layer obtained by cleaving the crystal at the [001] direction, which is the most common structure observed in the experiments. For comparison, we also considered the bulk structure. Due to the presence of *d* electrons, we used the DFT+U approach, with the Hubbard parameter set to 4 eV [6]. We chose this U value using the procedure described in SB Negedu et al. [21]. We tested U values ranging from 1 up to 6 eV and found that the electronic bandgap and the valence states values were only slightly affected by the correction in comparison to the calculation performed without the correction. However, there were moderate changes in the conduction bands due to the strong correlation observed in the d-states, where the correction was applied. **Figure S9** shows the band with and without the correction (for U=4 eV), which produces an electronic bandgap value closer to the experimental one. Additionally, we ensured that the magnetic energies calculated for different configurations were not significantly affected by the choice of U. The energy cutoff was set to 300 Ry, and the Monkhorst−Pack scheme with an 8 × 8 × 1 (25 × 25 × 1 for the electronic band structure calculations and projected density of states (PDOS)) and an 8 × 8 × 8 k-point mesh for layer and bulk, respectively [22]. We consider in the optimization process that equilibrium is reached when forces on each atom are less than 0.01 eV/Å.

The formation energy E_f for each layer or bulk was calculated using the expression:

$$E_f = \frac{\left(E - \left(\frac{N_{Mn}\, E_{Mn}}{N_{Te}\, E_{Te}}\right)\right)}{N} \quad (1)$$

where E is the total energy of the system, $E_{Mn(Te)}$ is the energy of isolated Mn(Te) atom, $N_{Mn(Te)}$ is the number of Mn(Te) atoms, and N is the total number of atoms.

For each structure, we calculated the magnetic order from the expression:

$$\Delta E = E_{ferro} - E_{antiferro} \quad (2)$$

where $E_{ferro/antiferro}$ is the total energy value for the ferro/antiferro configurations. The system is ferro if ΔE<0 and antiferro for ΔE>0.

In order to obtain the heat capacity at pressure constant as a function of temperature, we use the SIESTA software to calculate the forces required as input used in PHONOPY software [23]. This software is based on the quasi-harmonic approximation used for thermal expansion, and then heat capacity is obtained.

3.0 Results and discussion

3.1 Structural, morphological and optical property discussion

Flame melting of the MnTe samples was carried out using acetylene flame as the melting point of the sample was 1170 °C. The bulk MnTe samples are polycrystalline with a hexagonal structure, P63/mmc group, with lattice parameters a=b= 4.23 Å, c= 5.95 Å. MnTe crystallizes in a Ni-As structure with hexagonal D_{6h}^4, closed-packed anions with octahedral holes filled with cations. Chemical and crystal structure instabilities were observed in the initial flame-melted sample due to Te/Mn ion migration and Mn oxidation, which resulted in MnO and $MnTe_2$ impurity phases being formed at times [24]. X-ray diffractograms show MnTe hexagonal peaks as the primary phase, with a $MnTe_2$ peak present for bulk samples before homogenization. Later the samples were homogenized at 900 °C for 10 hours. The bulk samples had pure MnTe peaks after homogenization, and we observed a hexagonal phase (JCPDS card numbers *01-086-1022, 03-065-5009*)

formation in the sample. XRD of exfoliated MnTe (**Figure 1b**) resulted in similar corresponding peaks but varied peak intensities compared to its bulk counterpart. The exfoliated 2D sheet contains more of a 001-type orientation.

Later, the as-cast and homogenized samples were surface polished with ethanol as water/dry polishing led to surface oxidation and breakage of the samples. The samples were highly brittle, and pits were formed during polishing. MnTe as-cast samples were nearly dense, and the Energy Dispersive X-Ray Spectroscopy (EDS) analysis showed that the sample's composition was 46.25 at% and 53.75 at% before homogenization, as seen in **Figure S1,** the compositional analysis after homogenization showed that the samples were near stoichiometric ratios (48.87 at% and 51.13 at%). Brittle samples are comparatively easier to exfoliate. Homogenized bulk MnTe samples were then powdered manually with mortar and pestle and dispersed in ethanol by sonication before drop cast. Exfoliated and bulk samples were both drop-casted on carbon tape for SEM and EDS analysis. The EDS analysis showed that the exfoliated composition varied from the as-cast, and there was a decrease in Mn and an increase in Te atomic percent in the sample (**Figure S2**). This is due to the exfoliation conditions that induce the sample breakage at weaker bonds and exfoliate layers of Te comparatively more than Mn at different planes.

The atomic arrangements of Manganese (Mn) and Tellurium (Te) are visible in the high-angle annular dark-field scanning transmission electron microscopy (HAADF STEM) images in **Figure 1c and 1d**. The FFT pattern extracted from the HAADF STEM image is shown in **Figure 1c,** the **inset** reveals the *hcp* pattern. **Figure 1d** shows lattice fringes with an interplanar distance of 0.3 nm corresponding to (103) plane, which was exfoliated in excess (from XRD). From the profile mapping of lattice fringes, the atomic radii are 197 pm, corresponding to Mn atoms in the particular orientation (**Figure 1d, inset**). To analyze the thickness, atomic force microscopy (AFM) was employed. AFM images showed flakes distributed over a wide scan area in **Figure 1e**. We could observe layered flakes of ~4 nm thickness which were overlapped. The average thickness of the exfoliated flakes was approximately 2-8 nm.

Later, the exfoliated samples and the bulk MnTe were analyzed for their optical properties. UV-visible absorption spectra were obtained in the range of 200 up to 1100 nm (**Figure S3a**). The bulk MnTe samples show no absorption peak, whereas the exfoliated MnTe sample had a broad absorption peak at 250 nm until 400 nm. Both samples' bandgap (E_g) were analyzed with the Tauc plots (**Figure 2a**). The graphs show that the E_g of the bulk sample was 1.79 eV, and the E_g increased to 2.80 eV for exfoliated samples due to the confinement effect. Both the samples lie in the semiconductor regions based on these optical bandgap measurements. Raman spectroscopy results were obtained for exfoliated 2D MnTe sample (**Figure 2b**) in the range of 100 up to 250 cm^{-1} at RT, with a laser excitation of 532 nm. Peaks were observed at 140 cm^{-1}, which are attributed to E_{2g} Raman active modes in MnTe bonding. It confirms the formation of MnTe, and the peaks have been consistent with the reported values. The other intense mode A_1 was shifted to 124.35 from 120.3 cm^{-1}. This shift in peak is a common attribute of lower dimensional materials due to weak interaction among the layers. Raman shift depends on the various phonon modes and the number of layers [25, 26]. Raman peak representing E_u bond stretching for tellurium at 140 cm^{-1} has been suppressed in the exfoliated MnTe sample, confirming that there are no elementary crystalline tellurium precipitates on the sample surface. The Raman scattering modes generally increase significantly when the thickness of the layers is reduced, indicating the enhancement of phonon-phonon scattering as the thickness is decreased.

X-ray photoelectron spectroscopy (XPS) measurements were carried out to verify the chemical integrity of the exfoliated samples. **Figure 2c** shows the XPS survey spectra representing peaks centred at 641.02 and 652.8 eV corresponding to $2p_{3/2}$ and $2p_{1/2}$ of the Mn 2p line, with satellite peaks of the same. The results are consistent with the existing reported values of the MnTe thin films [27]. The spin-orbit splitting energy (ΔSO) of the Mn 2p band is 11.74 eV in **Figure 2d**; the reported values were 11.49 eV for MnTe bulk. In Te 3d line, as seen in **Figure 2e**, two peaks at 573.24 and 583.76 eV correspond to $3d_{5/2}$ and $3d_{3/2}$, respectively, and the ΔSO of Te 3d band is 10.46 eV. The XPS spectra agree with reports of the NiAs-type MnTe [3].

3.2 Magnetic behavior of 2D MnTe

Superconducting quantum interference device (SQUID) measurements were carried out to obtain the magnetic properties of the Bulk and 2D MnTe. *M–H* curves of both bulk and 2D MnTe show magnetic ordering. MnTe is a well-known antiferromagnetic (*AFM*) material at room temperature [28-30]. From **Figure S4a**, the magnetic saturation (M_s) of the bulk MnTe was 0.34 emu g^{-1}. The sample shows no magnetic remanence (M_r) in bulk form.

As for 2D MnTe, the results show that there is a shift towards paramagnetic behavior (*PM*). The *M-H* curves of the 2D MnTe were measured at 300 K (RT) and 10 K (low temperature) with an applied field between −60 and 60 kOe. **Figure 3a** confirms the paramagnetic behavior, as a linear *M−H* relationship with a gradual increase in susceptibility was evident. These types of hysteresis curves are generally observed in low-dimensional paramagnetic materials. It has also been observed that the *M−H* loop does not saturate up to a field of 60 kOe (at RT), which is due to the predominant presence of the paramagnetic phase. Magnetic saturation (M_s) of 2D MnTe was measured to be 1.69 emu g^{-1} and 5.43 emu g^{-1} at 300 and 10 K, respectively. At lower temperatures, the magnetic ordering was disrupted, which resulted in the M_s value being 220% more than the RT values of 2D MnTe. 2D systems with continuous symmetry cannot be ordered, *i.e.,* spontaneous symmetry is difficult to break as fluctuations become more critical at lower temperatures. This shows that the paramagnetic behavior of the 2D sample was more evident at low temperatures.

The application of strain can turn non-magnetic materials into ferromagnets/paramagnets, as observed in chalcogenides [31, 32]. Extrinsic properties like oxidation states also contribute to magnetism and shape anisotropy enhances coercivity in a few tellurides [21]. We have obtained *FC-ZFC* data of both samples at zero field cooling (*ZFC*) from 350 to 10 K with zero fields, and data was recorded when cooling in the same field. After stabilization of the temperature, data were recorded when the sample was warming with a field of 1000 Oe. *FC-ZFC* curves for 2D MnTe are shown in **Figure 3b**. The *FC-ZFC* curves of 2D MnTe trace similar paths as bulk (**Figure S4b)** and have two transitions at 87 and 290 K and a transition around 37 K, which might be due to spiral-spin ordering in the material. The transition at 87 K is associated with *AFM* behavior with an anomalous behavior below 87 K [3]. There is a sharp increase in magnetization around 86.7 K in both the *FC-ZFC* curves as the temperature decreased, signifying ferromagnetic ordering, and this abrupt change of slope in the *FC-ZFC* curve is believed to be due to strong interplanar *FM* interactions as a result of magneto-elastic coupling. And the the Ńeel temperature (T_N) was shifted to 290 K for 2D MnTe, signifying the possibility of obtaining *PM* transition near room temperature. **Figure 3b: inset** shows inverse susceptibility curve, (χ^{-1}) shows compensation temperature (T_{cmp}) and spin reorientation temperature (T_{sr}) at 83.13 K and 87.28 K, respectively. *Curie–Weiss* behavior is often observed in *3d* metal compounds [34], manganese (Mn) element in our case. So we fit the χ^{-1} curves according to *Curie- Weiss* law (**Figure 3c** and **3d**) for both the sample. **Figure 3c** shows the x-axis intercept at *Curie-Weiss temperature* (θ_{CW}) which is equal to zero indicating paramagnetic behaviour of the 2D MnTe. And **Figure 3d** shows x-axis intercept at θ_{CW} to be in the negative region, this indicates *AFM* ordering with negative exchange interactions in the Bulk counterpart.

The temperature-dependent heat capacity (C_p) was measured by DSC to investigate the possible first and second-order transitions [35]. The C_p results for bulk and 2D MnTe samples are presented in **Figure 3e**. A single transition peak at ~305 K was observed for the bulk sample, whereas multiple transition peaks were observed for 2D MnTe. The second-order transition at the set temperature of ~305 K is due to the magnetic domain shift in the sample, signifying PM transition at this temperature. The same shift was observed at 286.5 K for 2D MnTe. Along with this, first-order transitions are observed at 294 K due to structural phase transitions in the sample, as it reaches lower dimensions during exfoliation. The results are also consistent with the *M-T* curves for both 2D and bulk MnTe (**Figure 3b** and **S4c**). Flake resistance was also measured by four-probe method to understand the contribution of individual elements in the sample (**details in SI**). **Figures S5a** and **S5b** show the electrical conductivity and corresponding electrical resistance of the exfoliated sample, respectively, calculated through the four-probe method. Considering the average flake dimensions from the AFM images, the average flake resistance was calculated to be 1.46 μΩ (average flake thickness ~4 nm). We confer that there was no significant contribution from individual Mn or Te flakes toward magnetic or electrical properties.

C_p value was also calculated using DFT for bulk and 2D MnTe sample at constant pressure. We observe C_p increasing until 288 K for bulk sample, which corresponds

to phase transition at 304 K (**Figure S4c**). For the 2D MnTe the second transition was observed at 316 K. The first transition for both bulk and 2D sample was at 87 K, this transition corresponds to linear behavior of C_p until 93 K. Therefore in **Figure S4c** we see three distinct behaviors: linear until close to 93 K where bulk and 2D MnTe are both very similar, later we observe an increased logarithmic behavior with the maximum at 288/316 K for bulk/2D MnTe and from this we observe one decrease for both cases. We believe that the maximum can be related to transition that is close to the T_N. **Figure 3f** shows recent 2D Mn-based chalcogenides whose magnetic susceptibilities (M_s) are comparable with our synthesized 2D MnTe at RT and lower temperature [10 K] [36]. The M_s of bulk MnTe were also greater than many doped Mn systems like $KMnTe_2$, $RbMnTe_2$, $Na_3Mn_4Te_6$ and so on [37].

3.3 Simulation results

Figure 4a presents the electronic band structure calculations for the MnTe bulk and exfoliated layers. We plotted the bands separately to better visualize the different contributions of the majority and minority spin occupations. Except for the bulk case, the spin contributions produce different effects on the electronic bands for the other cases. We can see a "competition" between two different spin occupations. The minority spin occupation tends to transform the system into a metallic structure. In contrast, the majority spin occupation favours a semiconducting behavior. The electronic band gap values are typical of semiconductors for bulk and mono-layer case. Both are indirect, 0.9 eV and 1.4 eV, from Γ to M and Γ to X for bulk and one-layer, respectively. It should be stressed that GGA-PBE tends to underestimate the band gap values [38]. Note that in the layer cases, the band gap value for the majority spin decreases when the number of layers increases due to the quantum confinement effect.

Figure 4b shows the projected density of states (PDOS) of the atomic orbitals s (blue), p (red), and d (green) for the majority and minority spin occupations. For the bulk case, we can see that the majority and minority spin occupations have the same weight in the states producing an antiferromagnetic configuration (AF). We calculated the energy difference using the expression (2), and the result is positive 117.3 meV. We also calculated the bulk magnetic moment and obtained the null value, as expected for AF configurations. It agrees with experimental results where the magnetic behavior of bulk is minimal compared to layers. For the case of one layer, we do not compute the energy difference because the minimal number of metal atoms should be 2. But we confirmed from the PDOS an unbalance between minority and majority spin occupations, resulting in a ferromagnetic configuration (F) in the following form. For the other two cases of two and three layers, we observed the same ferromagnetic order F of one layer. The energy differences in both cases are negative, -46.6 and -36.1 meV for two and three layers, respectively. These energies, calculated using equation (2), are shown in **Figure 4** in the projected density of states. In the case of three layers, there are three different AFM configurations, but we only show the energy difference for the most stable configuration in **plot 4-(h)**. The energy differences for the other two AFM configurations are -67.5 meV and -70.4 meV, respectively.

In order to obtain the magnetic energy given by **Equation 2** for the case of one layer, we replicate the unit cell to create two different supercells composed of two and four Mn atoms. In **Figure S6** in the **supplementary information**, we present the different magnetic configurations considering up and down spins for the case with two (**Figure S6a**) and four (**Figure S6b**) Mn atoms. In **Figure S6b** we present the cases of one ferromagnetic and three non-similar antiferromagnetic configurations.

Our results show that one layer is antiferromagnetic because the ΔE (**Equation 2**) values for all configurations are +10.7 and +29.3 meV for two and four atoms in the supercell, respectively. The **Table S1** presents the energy configuration values for the different Hubbard parameters.

In contrast to the bulk case where the magnetic moment is zero, we find that layers have the same value given by μ=2.5 μ_B/cell. We have verified that both the energy difference values between FM and AFM, as well as the magnetization value, do not change if we disregard the Hubbard correction by choosing U=0 eV. The only change occurs in the total energy from DFT calculations. This indicates that the Hubbard correction is not producing any spurious results.

We also can see that the MnTe bulk and MnTe layers have predominant contributions from only the *p* and *d* atomic orbitals. In the range considered in **Figure 4b**,

except for the bulk case where the minority and majority produce symmetric occupations, we can see that the *d* states are more anti-symmetric for the layers. They have contributed more to the magnetic behavior of the layers. We tested the magnetic behavior of 2D MnTe under an external strain regime and temperature effects by *ab initio* molecular dynamics. We did not obtain significant changes in magnetic moment value for these cases.

Finally, we calculated the absorption coefficients as a function of photon energy for bulk, one, and two layers. The results are presented in **Figure 4c**. We presented the absorption curves between different (minority and majority) spin occupations. As expected, we do not observe any difference between minority and majority spin occupations for the bulk case. Our calculations suggest an indirect electronic band gap close to 1 eV and having the same spin component contributions for the optical transition from Γ to M. This transition can be observed in **Figure 4c,** where the absorption coefficient starts to absorb close to 1 eV. Thus for the bulk case that electronic and optical gaps have the same values. In contrast, we observe a different tendency for layer cases where the spin component effects are more significant.

As we mentioned, competition exists between spin occupations producing different tendencies in the electronic and optical band gap values. For one layer, we can see from **Figure 4c** that the absorption coefficient for minority starts close to the value 2 eV, which corresponds to an indirect transition from Γ to X shown in **Figure 4a** for the band structure calculation. For the case of the majority, it starts close to 3 eV in **Figure 4c,** which is related to a direct transition from Γ to Γ shown in **Figure 4a** for the corresponding band structure. Similar behavior is observed for two-layer cases, where the minority starts absorbing before the majority. These values are very close to the experimental ones, estimated from the Tauc plots (1.8 and 2.8, for bulk and 2D MnTe, respectively). In order to verify if the bands have or not some relevance on the magnetic effect, we recalculated the bands for Mn, Te, Mn plus Te bonded and Mn plus Te unbonded vacancies. For this we consider a supercell with 64 atoms. In the **Figure S7** we represent the band structure calculations for vacancies cases. We note that bands are different in a one layer case without vacancies, although the same tendency is observed where the majority spin presents more narrow states close to the Fermi level in comparison with minority cases. The polarization is practically the same for 2D MnTe without vacancies, where the magnetization values are 2.43, 2.54, 2.47 and 2.47 μB/cell, for Mn, Te, Mn plus Te bonded and Mn plus Te unbonded, respectively. This indicates that the band changes for these cases, but the magnetic moment is practically the same because the system remains ferromagnetic. We did not obtain significant changes in magnetic moment value for these cases. In other words, the bands along with the defects and dislocations also contribute to the magnetic behavior of 2D MnTe.

We would like to stress that a direct comparison with the experimental data is not possible because the interaction with an externally applied magnetic field is not an option within the framework of the DFT code we used.

Figure S8a presents the MnTe bulk and 2D structures cleaved at [001] crystal direction for one and two layers. We have a hexagonal structure for one-layer cases like silicene and germanene, presenting a buckling of 0.9 Å. We noticed that the layers have covalent bonds with the neighbours for cases with two or more layers. The bond between Mn and Te, which have an ionic character, is about 2.7 Å. We also see that the formation energy decreases when the number of layers increases (**Figure S8b**), and these energy values are similar to other systems composed of transition metal [39]. We investigated the structural stability of 2D MnTe considering two temperature regimes: at T=0 k by phonon dispersion calculation and T=1000 K by *ab initio* molecular dynamics using an NVT ensemble. **Figure S8c** shows the phonon dispersion calculation: **i)** for the path Γ→X→M→Γ and the first **ii)** and the last **iii)** snapshots from *ab initio* molecular dynamics at 1000 K for a total simulation time of 2000 fs. The absence of negative frequencies in **Figure S8c (i)** is indicative of the structural stability at T=0 K. Besides, we have three acoustic modes close at Γ special point, the flexural mode with quadratic characteristics associated with the perpendicular modes and two longitudinal modes with linear shape associated with the 2D plane vibrations. The modes range from 1000 and 1500 cm^{-1}, corresponding to optical modes. We can see from the last snapshot from *ab initio* molecular dynamics simulations that even at high temperatures, the structure remains intact and present only some increased buckling due to thermal effects.

Conclusion

We have synthesized 2D manganese telluride (MnTe) using a scalable synthesis method consisting of melting followed by liquid phase exfoliation (LPE). Structural and morphological analyses confirmed the formation of 2D MnTe flakes from their bulk counterpart. An increased magnetic saturation of 400% was observed for the 2D samples. Enhanced magnetic behavior is observed in 2D MnTe and is attributed to the change in orientation of polarization due to induced defects and dislocations during LPE. Besides, from band structure calculation, we observe unbalanced spin majority and minority, resulting in a net magnetization, which also contributes to the origin of magnetic behavior. DFT results show an antiferromagnetic state for the bulk, but for the 2D structures, the unbalanced population of the spin populations' results in a paramagnetic state at near room temperature T_N. These results are in agreement with the experimental observations. Such materials can be effectively utilized in magnetic-based sensors and memory devices.

Competing Interests

The authors declare no competing interests.

References

[1] Tedstone A A, Lewis D J and O'Brien P 2016 Synthesis, Properties, and Applications of Transition Metal-Doped Layered Transition Metal Dichalcogenides *Chem. Mater.* **28** 1965–74

[2] Zeugner A, Nietschke F, Wolter A U B, Gaß S, Vidal R C, Peixoto T R F, Pohl D, Damm C, Lubk A, Hentrich R, Moser S K, Fornari C, Min C H, Schatz S, Kißner K, Ünzelmann M, Kaiser M, Scaravaggi F, Rellinghaus B, Nielsch K, Hess C, Büchner B, Reinert F, Bentmann H, Oeckler O, Doert T, Ruck M and Isaeva A 2019 Chemical Aspects of the Candidate Antiferromagnetic Topological Insulator $MnBi_2Te_4$ *Chem. Mater.* **31** 2795–806

[3] Puthirath Balan A, Radhakrishnan S, Neupane R, Yazdi S, Deng L, De Los Reyes C A, Apte A, Puthirath A B, Rao B M, Paulose M, Vajtai R, Chu C W, Martí A A, Varghese O K, Tiwary C S, Anantharaman M R and Ajayan P M 2018 Magnetic Properties and Photocatalytic Applications of 2D Sheets of Nonlayered Manganese Telluride by Liquid Exfoliation *ACS Appl. Nano Mater.* **1** 6427–34

[4] Hussain R A and Hussain I 2020 Manganese selenide: Synthetic aspects and applications *J. Alloys Compd.* **842** 155800

[5] Mermin N D and Wagner H 1966 Absence of ferromagnetism or antiferromagnetism in one- or two-dimensional isotropic Heisenberg models *Phys. Rev. Lett.* **17** 1133–6

[6] Gibertini M, Koperski M, Morpurgo A F and Novoselov K S 2019 Magnetic 2D materials and heterostructures *Nat. Nanotechnol.* **14** 408–19

[7] Dante J. O'Hara, Tiancong Z, Amanda H. T, Adam S. A, Yunqiu K L, Choong H L, Mark R. B, Siddharth R, Jay A. G, David W. McC, and Roland K. K 2018 Room Temperature Intrinsic Ferromagnetism in Epitaxial Manganese Selenide Films in the Monolayer Limit 2018 *Nano Lett.*, **18**, 5, 3125–3131

[8] Markus A, Md. Nurul H, Jeyakumar K, Shawulienu K, Somesh C. G, Héctor G. H, Xin H, Peter L, and Hannu-Pekka K 2021 Synthesis and Properties of Monolayer MnSe with Unusual Atomic Structure and Antiferromagnetic Ordering *ACS Nano*, **15**, 13794−13802

[9] Sharma R K, Rastogi A C and Singh G 2004 Electrochemical growth and characterization of manganese telluride thin films *Mater. Chem. Phys.* **84** 46–51

[10] Wang Q, Sun Q, Jena P and Kawazoe Y 2004 Antiferromagnetic coupling driven by bond length contraction near the Ga1-xMnxN film surface *Phys. Rev. Lett.* **93**

[11] Komatsubara T, Murakami M and Hirahara E 1963 Magnetic properties of manganese telluride single crystals *J. Phys. Soc. Japan* **18** 356–64

[12] Gu P, Sun Y, Wang C, Peng Y, Zhu Y, Cheng X, Yuan K, Lyu C, Liu X, Tan Q, Zhang Q, Gu L, Wang Z, Wang H, Han Z, Watanabe K, Taniguchi T, Yang J, Zhang J, Ji W, Tan P H and Ye Y 2022 Magnetic Phase Transitions and Magnetoelastic Coupling in a Two-Dimensional Stripy Antiferromagnet *Nano Lett.* **22** 1233–41

[13] Rahman S, Torres J F, Khan A R and Lu Y 2021 Recent Developments in van der Waals Antiferromagnetic 2D Materials: Synthesis, Characterization, and Device Implementation *ACS Nano* **15** 17175–213

[14] Zhang S, Xu R, Luo N and Zou X 2021 Two-dimensional magnetic materials: Structures, properties

and external controls *Nanoscale* **13** 1398–424

[15] Mori S, Ando D and Sutou Y 2020 Sequential two-stage displacive transformation from β to α via β′ phase in polymorphic MnTe film *Mater. Des.* **196** 109141

[16] Sethulakshmi N, Mishra A, Ajayan P M, Kawazoe Y, Roy A K, Singh A K and Tiwary C S 2019 Magnetism in two-dimensional materials beyond graphene *Mater. Today* **27** 107–22

[17] Kochat V, Apte A, Hachtel J A, Kumazoe H, Krishnamoorthy A, Susarla S, Idrobo J C, Shimojo F, Vashishta P, Kalia R, Nakano A, Tiwary C S and Ajayan P M 2017 Re Doping in 2D Transition Metal Dichalcogenides as a New Route to Tailor Structural Phases and Induced Magnetism *Adv. Mater.* **29** 1–8

[18] Puthirath Balan A, Radhakrishnan S, Woellner C F, Sinha S K, Deng L, Reyes C D L, Rao B M, Paulose M, Neupane R, Apte A, Kochat V, Vajtai R, Harutyunyan A R, Chu C W, Costin G, Galvao D S, Martí A A, Van Aken P A, Varghese O K, Tiwary C S, Malie Madom Ramaswamy Iyer A and Ajayan P M 2018 Exfoliation of a non-van der Waals material from iron ore hematite *Nat. Nanotechnol.* **13** 602–9

[19] Peng H and Perdew J P 2017 Rehabilitation of the Perdew-Burke-Ernzerhof generalized gradient approximation for layered materials *Phys. Rev. B* **95** 1–5

[20] Soler M, Artacho E, Gale J D, Garc A, Junquera J, Ordej P and Daniel S 2002 Soler2002

[21] Hu K, Wu M, Hinokuma S, Ohto T, Wakisaka M, Fujita J I and Ito Y 2019 Boosting electrochemical water splitting: via ternary NiMoCo hybrid nanowire arrays *J. Mater. Chem. A* **7** 2156–64

[22] Atsushi T, Laurent C, Isao T, Gilles H, 2010 First-principles phonon calculations of thermal expansion in Ti_3SiC_2, Ti_3AlC_2, and Ti_3GeC_2 *Phys. Rev. B*, **81**, 174301-1-6.

[23] Negedu S D, Tromer R, Siddique S, Woellner C F, Olu F E, Palit M, Roy A K, Pandey P, Galvao D S, Kumbhakar P and Tiwary C S 2022 Enhancement in magnetization of two-dimensional cobalt telluride and its magnetic field-assisted photocatalytic activity *Appl. Phys. A Mater. Sci. Process.* **128** 1–11

[24] Hooshmand Zaferani S, Ghomashchi R and Vashaee D 2021 Thermoelectric, Magnetic, and Mechanical Characteristics of Antiferromagnetic Manganese Telluride Reinforced with Graphene Nanoplates *Adv. Eng. Mater.* **23** 1–9

[25] Yamamoto M, Wang S T, Ni M, Lin Y F, Li S L, Aikawa S, Jian W Bin, Ueno K, Wakabayashi K and Tsukagoshi K 2014 Strong enhancement of Raman scattering from a bulk-inactive vibrational mode in few-layer $MoTe_2$ *ACS Nano* **8** 3895–903

[26] Park M, Choi J S, Yang L and Lee H 2019 Raman Spectra Shift of Few-Layer IV-VI 2D Materials *Sci. Rep.* **9** 1–8

[27] Yang L, Wang Z H and Zhang Z D 2016 Electrical properties of NiAs-type MnTe films with preferred crystallographic plane of (110) *J. Appl. Phys.* **119**

[28] C.F. Squire, Antiferromagnetism in Some Manganous Compounds 1939 *Phys. Rev.* 56. 922

[29] T.Komatsubaro, M. Murakanri and E.Hirahara, 1963 Magnetic Properties of Manganese Telluride Single Crystals *J. Phys. Soc. Jpn.* 18, 356

[30] N. Kunitomi, Y. Hamaguchi, S. Anzai, Neutron diffraction study on manganese telluride 1963 J. Phys. Soc. Jpn. 18, pp. 744-744

[31] Ma Y, Dai Y, Guo M, Niu C, Zhu Y and Huang B 2012 Evidence of the existence of magnetism in pristine VX_2 mono-layers (X = S, Se) and their strain-induced tunable magnetic properties *ACS Nano* **6** 1695–701

[32] Zhou Y, Wang Z, Yang P, Zu X, Yang L, Sun X and Gao F 2012 Tensile strain switched ferromagnetism in layered NbS_2 and $NbSe_2$ *ACS Nano* **6** 9727–36

[33] Madelung, O., Rössler, U. & Schulz, M. (Eds) MnTe: Crystal Structure, Physical Properties Vol. 41D (*SpringerMaterials*, Springer-Verlag, Berlin, Heidelberg, 2000)

[34] Sam M & Alannah M. H 2022 Tutorial: a beginner's guide to interpreting magnetic susceptibility data with the Curie-Weiss law *Commun Phys* **5**, 95

[35] Romanova O B, Sitnikov M N, Loginov Y Y and Hichem A 2022 Concentration dependences of the structural, magnetic and kinetic properties of manganese chalcogenides doped with tellurium *IOP Conf. Ser. Mater. Sci. Eng.* **1230** 012016

[36] Kim J, Wang C and Hughbanks T 1998 Synthesis and Structures of New Layered Ternary Manganese Tellurides: $AMnTe_2$ (A = Li, Na) *Inorg. Chem.* **37** 1428–9

[37] Gu P, Sun Y, Wang C, Peng Y, Zhu Y, Cheng X, and Ye Y 2022 Magnetic phase transitions and magnetoelastic coupling in a two-dimensional stripy antiferromagnet *Nano Letters*, 22 (**3**), 1233-1241

[38] Karazhanov S Z, Ravindran P, Fjellvg H and Svensson B G 2009 Electronic structure and optical properties of $ZnSiO_3$ and Zn_2SiO_4 *J. Appl. Phys.* **106**

[39] Liang Y, Yang J, Yuan X, Qiu W, Zhong Z, Yang J and Zhang W 2014 Polytypism in superhard transition-metal triborides *Sci. Rep.* **4** 1–5

Figures:

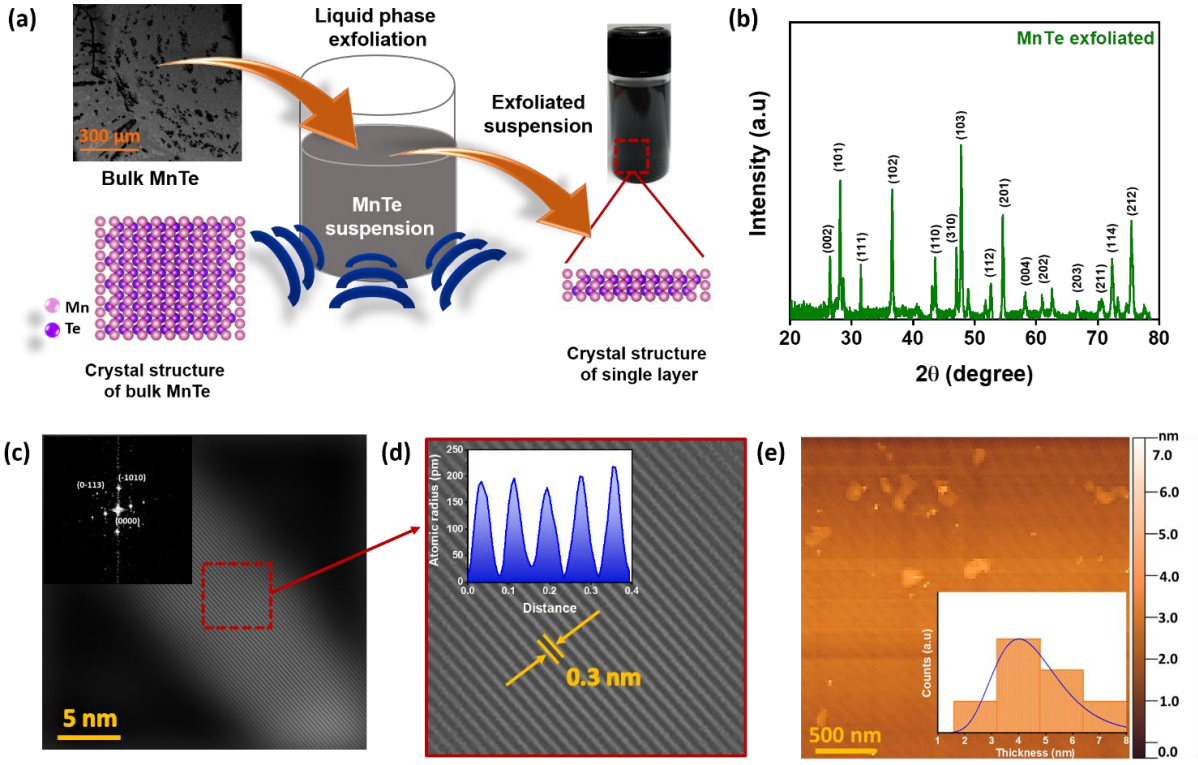

Figure 1: *(a) Schematic involving the synthesis protocol of Manganese telluride (MnTe), (b) X-ray diffractogram of the exfoliated sample, (c) HAADF-STEM image of MnTe exfoliated flake (inset: FFT pattern of the flake), (d) Lattice fringes from inverse FFT pattern (inset: atomic radius distribution) and (e) AFM image (inset: histogram plot showing the average flake size distribution).*

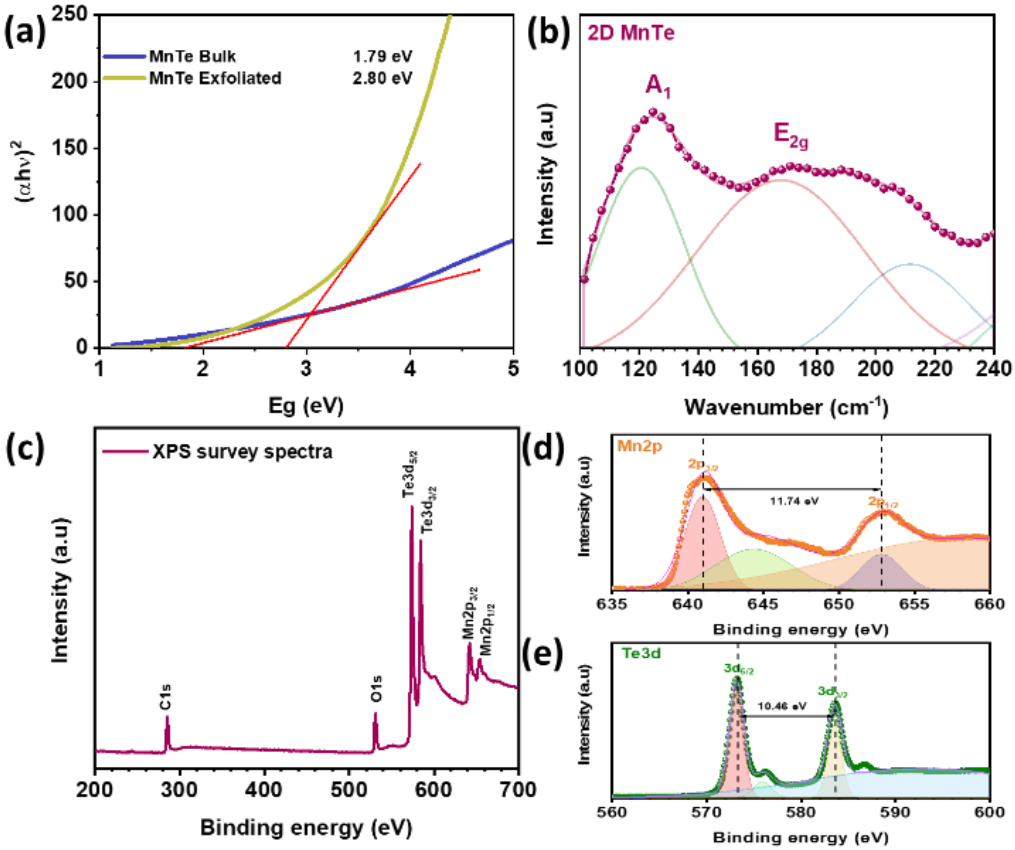

Figure 2: *(a) Tauc-plot of bulk and exfoliated MnTe, (b) Raman spectroscopic results of exfoliated MnTe, (c) XPS measurements of exfoliated samples, (d) Mn2p peaks and (e) Te3d peaks of the exfoliated sample.*

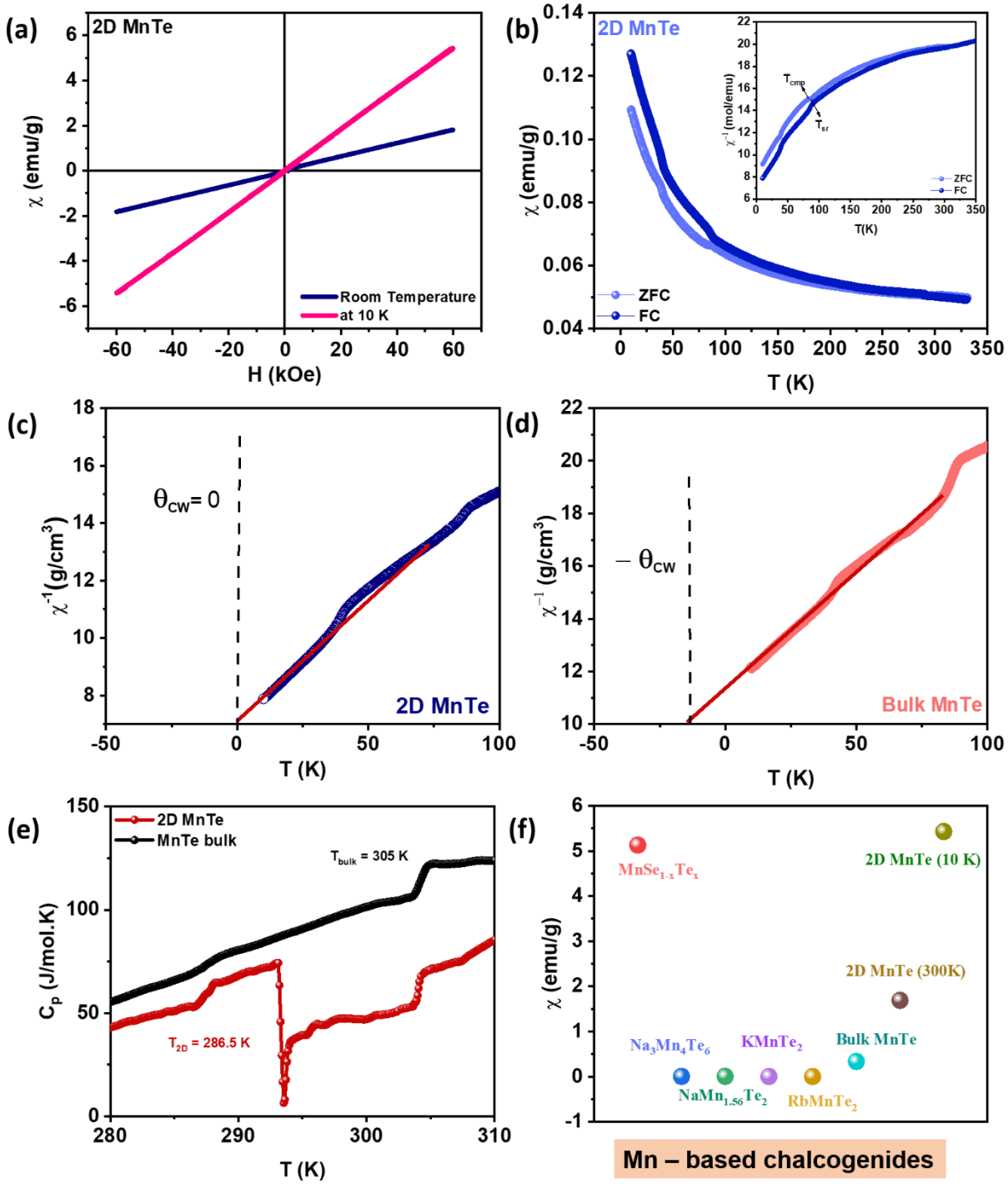

Figure 3: *Magnetic behavior of exfoliated MnTe flake (a) M-H loop at 10 K and 300 K temperatures, (b) 2D MnTe FC-ZFC M-T curve at 1000 Oe, Inverse susceptibility vs. temperature graph at 1000 Oe for (c) 2D MnTe and (d) bulk MnTe, (e) Heat capacity at pressure constant (C_P) as a function of temperature is calculated by DSC and (f) Comparison graph of magnetic susceptibility of other 2D Mn-based chalcogenides.*

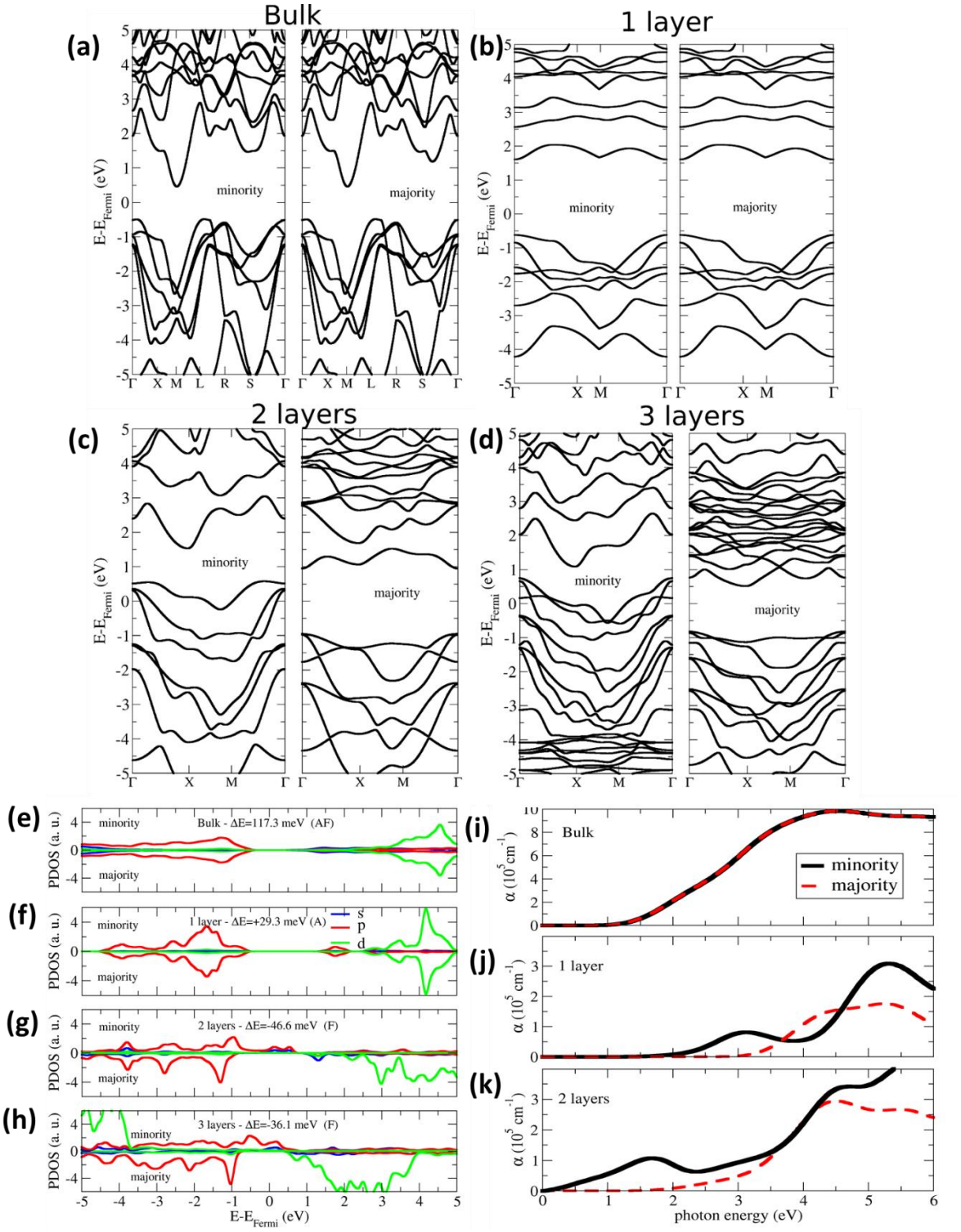

Figure 4:*(a-d) Bands structure calculation for MnTe bulk and exfoliated layers considering the majority/minority spin effects, (e-h) Project density of states on atomic orbitals for MnTe bulk and 2D layers separated in minority and majority spin occupations. The energy difference indicates the ferro (F) / antiferromagnetic order (AF) and (i-k) Absorption coefficient for bulk and layer as a function of photon energy considering the minority and majority spin occupations.*